Geochemical evidence for seabed fluid flow linked to the subsea permafrost outer border in the South Kara Sea.

Petr Semenov [1*], Alexey Portnov [2,3], Alexey Krylov [1,4], Alexander Egorov [5] and Boris Vanshtein [1].

[1] *All-Russia Institute for geology and Mineral resources of the world Ocean (VNIIOkeangeologia), Saint-Petersburg, Russia*

[2] *School of Earth Sciences, The Ohio State University, Columbus, Ohio, USA*

[3] *CAGE - Centre for Arctic Gas Hydrate, Environment and Climate, Department of Geology, UiT The Arctic University of Norway, Tromsø, Norway*

[4] *Saint-Petersburg State University, Institute of Earth Sciences, St. Petersburg, Russia*

[5] *Shirshov Institute of Oceanology, Moscow, Russia*

**Notices contact:* *Petr Semenov*

Email : petborsem@gmail.com

Phone: +79062634417

Address: *All-Russia Institute for geology and Mineral resources of the world Ocean (VNIIOkeangeologia)*

Angliyski Ave. 1, 190121 Saint-Petersburg, Russia

ABSTRACT

Thawing subsea permafrost driven by rising bottom water temperatures leads to a drastic increase in fluid flow intensity in shallow marine sediments, and consequently emission of methane into the water column. Dissociation of permafrost-related gas hydrates, as well as mobilization of permafrost-sequestered methane into the global carbon cycling are of primary importance for future Arctic Ocean acidification. Previous studies in the South Kara Sea showed that abundant hydro-acoustic anomalies (gas flares) induced by seafloor gas discharge into the water column are limited to the water depths ≥ 20 m. Such distribution of gas flares may indicate an outer extent of continuous permafrost spatially restricting the upward fluid flow. This study focuses on geochemical analysis of the 1.1 m long sediment core, acquired offshore Yamal Peninsula (South Kara Sea) in the area of shallow fluid flow recorded in the high-resolution seismic data. Our results show narrow zone of Anaerobic Oxidation of Methane (AOM) with sharp and shallow sulfate-methane transition (SMT) located at 0.3 m subbottom depth and significant temporal variations in methane discharge confirmed by pyrite (FeS_2) distribution. Concave up pore water chloride profile depicts an upward fresh/brakish

water advection in subsurface sediments. Terrestrial/fresh water genesis of interstitial methane from the sampled core is inferred from stable isotopic signatures (δ^{13} C and δD). We propose two possible mechanisms for the observed fluid flow: i) convection of thaw water from subsea permafrost, and/or ii) lateral sub-permafrost ground water discharge marking the outer limit of continuous permafrost extent offshore central Yamal Peninsula at ~45 m water depth.

KEY WORDS: Kara Sea, methane, permafrost, pore water, anaerobic oxidation of methane

INTRODUCTION

Most existing field observations and numerical models on subsea permafrost focus on the East Siberian (Shakhova et al., 2010; 2015), Laptev (Koch et al., 2009; Overduin et al., 2015) and Beaufort Sea shelves (Ruppel, 2011; Brothers et al., 2012; Frederick and Buffet, 2015; Dimova et al., 2015). The Kara Sea shelf is significantly less studied, however existing data show that continuous permafrost does not extend beyond the 20 m isobaths offshore Yamal Peninsula (Rekant and Vasiliev, 2011; Portnov et al., 2013; Portnov et al., 2014; Serov et al., 2015). This has been evidenced from the distribution of gas-related hydro-acoustic anomalies limited to water depth ≥ 20 m, which was hypothesized to mark the further extent of continuous permafrost spatially restricting upward gas migration. Offshore extent of subsea permafrost on the West Yamal Shelf is similar to the predicted Beaufort Sea shelf permafrost distribution (Brothers et al., 2012) suggesting similar scenarios of subsea permafrost evolution in these two regions.

Methane transport initiated by permafrost-induced fluid migration is of particular importance due to its contribution to atmospheric methane budget and its role in providing carbon source for local biogeochemical environment (McGuire et al., 2009). One of the important processes, which modulates methane transport through diagenetic zone is microbial-mediated anaerobic methane oxidation (AOM) coupled with sulfate reduction (SR) described by the following net reaction: $SO_4^{2-} + CH_4 = HS^- + HCO_3^- + H_2O$. AOM is responsible for removal of interstitial methane from marine sediments, providing a geochemical barrier for methane transport into the water column and the atmosphere. In the diffusion-based systems, steady-state AOM implies the inverse downcore profiles of sulfate and methane clearly indicating the sulfate methane transition (SMT), a depth interval where the reactants are entirely consumed with 1:1 stoichiometry (Iversen and Jørgensen, 1985; Jørgensen, 2006). On the contrary, elevated upward methane flux in advection-based systems shifts the SMT closer to the seabed indicating active methane seepage (Borowski et al., 1996; Coffin et al., 2013).

In this study, we present the results of geochemical analyses on the sediment core recovered within the area of focused fluid flow offshore Yamal Peninsula in the South Kara Sea (Fig. 1). We interpret the results of geochemical and biogeochemical analyses of near-surface sediment section affected by methane discharge in context of subsea permafrost degradation as the most significant prerequisite for fluid migration on the South Kara Sea shelf. We infer that the effect of permafrost on

subsurface fluid migration in our study area may be explained by two fundamental mechanisms: i) convection of thawing water transporting the syngeneic constituents and ii) migration from remote non-permafrost sources initiated by subsea permafrost degradation.

Data and Methods

The data used in the current study were collected during a cruise conducted by All-Russia Institute for Geology and Mineral Resources of the World Ocean ("VNIIOkeangeologia") in 2012 on board RV "Neotrazimy" in the framework of the state program "Perennial Comprehensive Seabed Geological Survey of Coastal Yamal Shelf". During the cruise, we acquired 127 bottom coring stations, including station T-04, which was chosen for detailed analysis (Fig.1a).

High-resolution seismic (HRS/chirp)

HRS/Chirp data were acquired with EdgeTech 3100 SB-216S sub-bottom chirp profiler. Frequency range of 2-14 kHz, 20 ms pulse duration and 0.25 sec pulse range provided ~0.5-1 m vertical resolution and at best 20 m penetration. Swell filter and automatic gain control were applied to raw chirp data, allowing for better visualization of the upper sediment section.

Sediment sampling

Bottom sampling station T-04 (71° 50' 56.7579" N; 67° 11' 49.4381") is located offshore Yamal Peninsula in the South Kara Sea in the water depth of 45 m. Sediment core (110 cm long) was recovered using the conventional gravity corer with 127 mm diameter and 1.5 m length, containing the plastic insert. Subsea positioning of the gravity corer during the deployment was provided by the calibrated hydroacoustic system HiPAP 350 P-5 (Kongsberg) with ultra short baseline configuration (USBL) providing accuracy ± 0.5 m.

After obtaining the gravity corer on deck, the plastic insert containing the core was extracted from the pipe. In order to minimize the loss of interstitial gases and to protect the reduced porewater compounds from oxidation, the core was cut into two halves longitudinally. One part was immediately subsampled for geochemical analysis, while the other part was placed in the onboard geological lab for visual description. Geochemical sampling was performed from seven horizons: 5, 10, 30, 45, 60, 90, 110 cm below the seafloor (cmbsf).

Grain-size analysis

The grain size analysis was performed by a combination of sieve (sand and silt fraction) and pipette (settling of clay particles according to the Stokes law) methods (e.g. Krylov et al., 2005). The amount of sand (1-0.05 mm), silt (0.05-0.005 mm) and clay (<0.005 mm) fractions (in accordance with the classification by Rukhin (1961)) were estimated (Lapina, 1977).

Mineralogical analysis

Aleurite fraction (0.05-0.1) was used for determination of sedimentary mineral composition. Light and heavy minerals were separated by weighting in separatory funnels filled with $CHBr_3$

(ρ=2.84-2.86). Filtered, dried and weighed samples were carefully smeared on slide in immersion oil so that 300-400 mineral grains became visible in Olympus BH-2 microscope. Light minerals were studied at magnification x200 using the immersion oil with refraction index 1.542-1.544. Heavy minerals were split in two parts and analyzed at the same or lower magnification using two types of immersion oil with refraction indices 1.700 -1.706 and 1.638-1.640. Mineral species were determined based on their morphology and optical properties (Sakharova and Cherkasov, 1970), specified minerals were counted visually and quantified in % from the total aleurite fraction (Lapina, 1977).

Sedimentary TOC (Total Organic Carbon)

Sediment samples were frozen at -20 °C by means of ScanVac Coolsafe 1100 lyophilizer prior to onboard freeze-drying. Dried sediments were homogenized by Retch RM200 grinder. TOC content was measured using Shimadzu TOC-V CSN element analyzer equipped with Solid Sample Unit SSM-500A in an onshore lab.

Sedimentary gas extraction

Interstitial gas samples were extracted with the degassing set SUOK-DG (Patent (19) RU (11) 2348931 (13) C1) including centrifugal pump, supersonic ejector and hollow stainless steel working volume. Pre-weighted sediment samples were loaded into the sampling chamber and completely re-suspended by degassed water under high pressure. Interstitial gas phase was separated from the homogenous sediment pulp by supersonic ejector and fed into the graded volume meter. After the volume measurements, isolated sedimentary gas was transferred into the crimped vials with butyl-rubber stoppers (Portnov et al., 2018).

Interstitial methane and C_2-C_5 hydrocarbon (HC) gases

Hydrocarbon (HC) gas composition (C_1-C_5) including 8 compounds (Table 1) was analyzed using Shimadzu 2014 gas chromatograph (GC) equipped with flame ionization detector (FID) and Restek Rt-Aluminia BOND/Na_2SO_4 wide-bore capillary column (i.d. 0.53 mm, length 50 m, film thickness 10 μm) attached to the packed injector. Helium was used as a carrier gas at a flow rate of 25 ml/min. Certified gas mixtures were used as external standards. The detection limit of the analysis was 50 ppb, for CH_4 the error of instrumental measurements did not exceed 5%.

Sedimentary n-Alkanes and isoprenoids (C_{10}-C_{40})

For determination of n-alkanes and isoprenoids (phytane and prystane) sediment samples were freeze-dried onboard, grinded and stored dry until the on-shore lab analysis. Hexane extraction of the total liquid hydrocarbons (HC) was performed using Soxterm SOX 16 system (Gerhardt). Extracts were rotary evaporated, the resulting dry residue re-suspended in 2 ml of hexane and transferred into a 2 ml vial with PTFE screw caps. GC-FID analysis was carried out on Shimadzu GC 2014 using Machinery Nagel Optima-1 capillary column (0.25 mm, 30 m) and helium as a carrier gas (1.5 ml/min flow rate). Samples were injected using Shimadzu AOS 20i autoinjector. Splitless mode of

GC evaporator retained during 1 min after withdrawal of a syringe needle and split vent re-opened to provide a ratio 1:20. The GC oven was programmed from 100°C to 320°C at 6 °C/min. Additional flow of carrier gas (make-up) was supplied to FID at a rate 25 ml/min. Certified mixture of odd and even C_{10}-C_{40} n-alkanes and isoprenoids (Chiron) was used as external standard for quantification, aliquote of squalane was spiked into sediment sample prior to extraction for evaluation of HC recovery during sample preparation. The analytical precision estimated on multiple injections was within a range of 2-8%.

Pore water sulfate and chloride

Sedimentary pore water was extracted by wet sediment centrifugation 6240 G using Haereus Megafuge 1 at in 50 ml plastic centrifugal tubes flushed with argon stream to minimize the pore water sulfide re-oxidation. Pore water samples represented by supernatants were filtered through a 0.25 um glass microfiber syringe filter (GF/F) and transferred into a 2 ml Eppendorf tubes allowing no headspace and stored frozen until the onshore instrumental measurements.

Anions concentrations were measured using the Metrohm 940 Proffesional IC Vario ion chromatograph equipped with conductometry detector, MSM-A rotor suppressor unit and Metrosepp A Sup 5 -150/4.0 column. Samples were eluted by 5 mmol Na_2CO_3/$NaHCO_3$ solution at 1 ml/min flow rate. Prior to analysis, pore water samples were diluted 1:50 to reduce the seawater chloride level overloading the column. The minimum detection limit of the applied method was 10 ppb (for both anions), while the error did not exceed 4 %.

Total Alcalinity (Talk)

Pore water samples were filtered through a 0.25 um glass syringe microfiber filter (GF/F) into 10 ml borosilicate vials. Total Alcalinity (Talk) was determined by titration of pore water samples against H_2SO_4 with indication by phenolphthalein and methyl orange at pH 8.3 and 4.4 respectively. pH was measured by Hanna HI 83141 pH-meter.

Stable isotopic composition of carbon and hydrogen in methane.

The isotope measurements were performed by isotopic-ratio gas chromatography/mass spectrometry (GC/IRMS). The minimum methane concentrations required for measurements were 20 ppmV and 200 ppmV for determination of $^{13}C/^{12}C$ and $^{2}H/^{1}H$ respectively.

Carbon isotope composition ($^{13}C/^{12}C$) in CH_4 was measured with an Agilent 6890N GC (Agilent Technologies, Santa Clara, US) interfaced to a Finnigan Delta S IRMS (Bremen, Germany) using a Finnigan GC-C II interface. The GC was equipped with Molsieve column (12 m, 0.32 mm i.d.) and an injection valve. Samples were calibrated against a certified standard; the resulting isotopic signatures were reported in δ notation and per mil (‰) values vs. VPDB ($\delta^{13}C$ VPDB).

The hydrogen isotope measurements ($^{2}H/^{1}H$) were performed on an Agilent 7890A GC (Agilent Technologies, Santa Clara, US) interfaced to a MAT 253 IRMS (Thermo Scientific,

Bremen, Germany) using a GC-Isolink interface by Thermo.The GC was equipped with Molsieve column (12 m, 0.32 mm i.d.) and an injection valve. Samples were calibrated against a certified standard; the resulting isotopic signatures were reported in δ notation and per mil (‰) values vs. VSMOW as (δD VSMOW)

Results

High-resolution seismic (HRS/chirp)

A sub-seabed seismic amplitude anomaly, which was chosen for sediment coring (Fig. 1b), is a ~120 m wide amplitude blanking zone, extending upward from the subbottom depth of >25 m and reaching the seafloor in the water depth of 45 m. We interpret this amplitude anomaly as a zone of focused vertical gas discharge, indicating active fluid flow in this area.

Lithology and grain size composition.

The upper part of T-04 sediment core (5-25 cmbsf) is formed by black clayey silt with H_2S odor and insignificant admixture of shelly detritus (Fig. 1c). Downwards, in the interval 25-105 cmbsf, the core comprises a layer of dark-grey clayey silt with inclusions of hydrotroillite. Grain size composition changes from 6.5% of sand, 54.0% of silt and 39.4% of clay in the upper 5 cm thick horizon, to 59.9 % of sand, 20.0 % of silt and 19.9% of clay in the bottom of the core (110 cmbsf). The strongest changes in proportion of the grain-size fractions characterize the interval between 60 and 110 cmbsf (Fig. 1c).

TOC

Maximum TOC content along the core is measured at 5 cmbsf (0.67% wt). In 5-45 cmbsf interval, TOC profile demonstrates almost constant value (0.63-0.67%), while deeper in the section, we observed gradual depletion reaching minimum value 0.2 % at 110 cmbsf (Fig. 2a).

Composition of n-alkanes and isoprenoids (C_{10}-C_{40})

n-Alkanes and isoprenoids were analyzed in the sediment sample from the uppermost horizon (5 cmbsf) containing recently deposited organic matter (OM). There is a unimodal distribution of the measured compounds with conventional predominance of odd homologues C_{27}-C_{31} (Fig. 2c) derived from terrigenous vascular plants waxes (Peters et al., 2008). Terrigenous constituent represented by n-alkanes of C_{25}–C_{34} series is characterized by carbon preference index (CPI C_{25}-C_{34} = $(C_{25}+C_{27}+C_{29}+C_{31}+C_{33})$ / $(C_{24}+C_{26}+C_{28}+C_{30}+C_{32})$ + $(C_{25}+C_{27}+C_{29}+C_{31}+C_{33})/(C_{26}+C_{28}+C_{30}+C_{32}+C_{34})$=5,05) indicating an odd overprint of recent OM and no signs of migrated petrogenic constituent (Abrams, 2005). Low molecular weight fraction (C_{14}-C_{34}) associated with autochtonous organic matter in oligotrophic conditions of the Kara Sea is mainly supplied to the bottom sediments by primary production (Stein and Fahl, 2004; Vetrov and Romankevich, 2011). Terrigenous/aquatic index (TAR= $C_{27}+C_{29}+C_{31}/C_{15}+C_{17}+C_{19}$=10, 5) demonstrates the major contribution from terrigenous source and minor from in situ production (Bourbonniere and Meyers, 1996). Isoprenoid ratio (Pr/Ph=0.1) suggests

anaerobic or poorly oxygenated depositional environment (Peters et al., 2008).

Methane and C_2-C_5 hydrocarbon gases

The lowermost sampling horizon (110 cmbsf) shows maximum methane concentration reaching 734 μM. In contrast, minimum concentration (0.87 μM) is observed in the uppermost core section (5 cmbsf) (Table 1). The CH_4 concentration plot exhibits sufficient variations along the sediment section (Fig. 3). The steepest gradient is obseved in the interval 30-10 cmbsf. Despite the strong H_2S odor, visual analysis of sediment core T-04 revealed no gas-induced cracks, voids or other features of interstitial gas oversaturation and ebullition. Maximum measured concentration/saturation of interstitial methane (0.734 mM) is twice lower than the saturation limit for dissolved methane at atmospheric pressure (~1.3 mM) (Yamamoto et al., 1976; Jørgensen et al., 2001).

The relatively insignificant percentage of C_{2+} compounds in the total HC gas composition (e.g. 0.03% at 110 cmbsf) suggests microbial origin of methane (Whiticar 1999; Abrams, 2005. The ratio of methane concentration to the total content of gaseous hydrocarbons ($C_1/\Sigma C_2$-C_5) shows significant upward decrease from 3452 at 30 cmbsf to only 22 at 5 cmbsf (Fig. 3, Table 1).

Pore water sulfate and chloride

Sulfate distribution shows significant decrease with depth from 25.1 mM at 30 cmbsf to 1,38 mM at 110 cmbsf (Fig.3). The corresponding downcore profile is of concave up shape (Fig. 3).

Chloride profile reveals the downcore depletion from 536.3 (5 cmbsf) to 121.87 (110 cmbsf) (Fig. 3).

Total alkalinity (Talk)

The lowest Talk value (~7 mM) was measured in the uppermost interval 5-10 cm (Fig. 3). Below, it is characterized by a sharp downcore increase to 15.44 mM within 10-30 cmbsf, followed by a decrease from 12.27 to 10.75 mM within 45-110 cmbsf interval.

Sedimentary mineral composition

Content of authigenic minerals, including carbonates and pyrite, which formed as a result of the net sulfate reduction, is of a particular interest in the current study. Among carbonates we were only able to detect trace amounts of siderite (< 0,2%) with uniform distribution within the sampled sediment section.

Downcore pyrite concentration/content shows drastic increase within the 30-45 cmbsf interval. The highest concentration of 55.4 % (aleurite fraction) was measured at 30 cmbsf (Fig. 3). Above and below this interval the values of pyrite are within the background range of 0.8-5.4 %. Light microscopy showed that framboid made up the obviously predominant textural form of pyrite in the samples from 30 and 40 cmbsf enriched in this mineral. Morphological analysis indicated the primarily authigenic nature of pyrite in the sediments of T-04 core .

Stable isotope composition of carbon and hydrogen in methane.

Carbon isotopic signatures ($\delta^{13}C$) of CH_4 range from -77.8 to -79.9 ‰ VPDB (Fig. 3). Hydrogen isotopic signatures (δD) vary from -296 to -281 ‰ VSMOW. $\delta^{13}C$ and δD values remain almost constant along the sediment core (Table 1). Methane content in the gas samples from the uppermost horizons (5 and 10 cmbsf) was not sufficient for the isotopic measurements.

Discussion

Sources of the organic matter and their significance for early diagenesis

Sediments of the West Yamal coast and adjacent shallow shelf undergo intensive coastal erosion, which results in the delivery of allochtounous OM (Stein and Fahl, 2004). OM enriched with terrigenous compounds is refractory to biochemical reactions and mostly preserved during early diagenesis (Stein and Fahl, 2004; Vetrov and Romankevich, 2011). In turn, contribution of fresh and reactive autochtonous OM, linked to the aquatic primary production is relatively low due to low productivity of cold and shallow waters of South Kara Sea. This portion of OM is presumably consumed by aerobic oxidation within the water column and at the seafloor. Thus, only few percent of the initial amount is left for anaerobic diagenesis (Vetrov and Romankevich, 2011; Rozanov, 2015). TOC content of 0.68% wt measured beneath the oxidized layer (5 cmbsf) in core T-04 is a typical regional background value for the Kara Sea shelf (Stein and Fahl, 2004; Seiter et al., 2014; Rozanov, 2015). However, the downward decrease in the sedimentary TOC is likely attributed to the lithological control rather than the OM mineralization. This becomes evident from the correlation between the TOC content and percentage of clay fraction (Fig 2b) retaining OM due to its high sorption capacity (Tyson, 1995; Secrieru and Oaie, 2009). Such mechanism causes a consistent lithologicaly controlled partitioning of sedimentary TOC and its downcore variations.

Results of our analysis of sedimentary lipid biomarkers (n-alkanes and isoprenoids) in the uppermost sampling interval (5 cmbsf) show significance of OM sources for the studied depositional environment. We observe prevalence of terrigenoous OM indicated by unimodal distribution pattern of n-alkanes with domination of C_{29}, C_{31} and C_{33} odd homologues. Contribution from C_{14}-C_{25} compounds representing the liable autochtonous OM in our samples is low to moderate (Fig 2c) (Meister et al., 2013; Vetrov and Romankevich, 2011). The drastic predominance of terrigenous organic matter does not provide favorable conditions for intensive organoclastic sulfate reduction (OSR) in the T-04 upper anoxic sediments, which may cause the detected subsurface sulfate depletion within 110 cmbsf (Jørgensen et al., 2001; Jørgensen, 2006; Meister et al., 2013).

Methane, sulfate and AOM

Results of our analyses from 126 coring stations show the average value of sedimentary methane concentration 4.58 μM in the interval 85-120 cmbsf (n=126). This concentration may be used as a reliable background value for T-04 core, because the methodology of gas measurements was identical at all sampling locations. Measured maximum of methane concentration at the

corresponding depth of 110 cmbsf in T-04 core (734.2 μM) is 158 times higher than the background value, indicating focused methane-rich fluid flow in our study area.

Methane $\delta^{13}C$ values in T-04 core range from -77.8 to -79.9 ‰ VPDB suggesting its microbial genesis. Additionally, gas composition in the samples with high methane content (i.e. less altered by the AOM) shows only trace input of heavy homologues, which is also typical for microbial source (Table 1) (Abrams, 2005). Yet, possible minor admixture of thermogenic gas should not be ruled out (Whiticar, 1999).

The inverse trends of sulfate and methane profiles (Fig. 3) indicate process of AOM in the bottom sediments (Iversen and Jørgensen, 1985). However, a concave-up sulfate profile in T-04 does not correspond with typical steady state AOM profile, characterized by the linear gradient of pore water sulfate, depicting the diffusive flux into the reaction zone (Iversen and Jørgensen, 1985; Borowski et al., 1996; Jørgensen et al., 2001). The subsurface concave up sulfate profiles are normally attributed to the OSR-dominated conditions, which is definitely not characteristic for T-04 depositional environment. Therefore, it is evident that sulfate concentration in our study area is strongly affected by an external process. (Iversen and Jørgensen, 1985).

Hydrogen sulfide, produced by SR including both OSR and AOM, interacts with either dissolved iron or reactive solid-state iron oxides forming the precipitate of amorphous iron sulfide (FeS), which may successively convert to pyrite (FeS_2). This mineral is stable enough to be preserved in the sediments for many millennia; therefore it presents a reliable proxy for paleo-environmental reconstructions (Sassen et al., 2004). Overproduction of pyrite is reported to mark the shallow SMT indicative of transitional diagenesis from lower to higher methane supply with corresponding redistribution of reactive compounds (Lin et al., 2016; Coffin et al., 2008). At the same time, there are examples of methane seepage settings in which pyrite precipitates above the thin zone of subsurface iron reduction, but not within the SMT. In this case, iron sulfide formation is restricted by spatial pattern of reactive Fe (II) concentration, as opposed to a more typical scenario when pyrite crystallization is restricted to the local discharge of H_2S as result of AOM (Latour et al., 2018).

Downcore profile of the sedimentary pyrite (FeS_2) in T-04, shows sufficient selective accumulation of this mineral within the depth interval 30-45 cmbsf (Fig. 3). Wherein, its maximum at 30 cmbsf (55.4% of the net heavy minerals composition) appears to coincide with the maximum of pore water $Talk^-$(15.44 mM), reflecting the release of the SR products (HCO_3^{2-} and HS^-). Given that AOM is a major driver of SR, this subbotom depth (30 cmbsf) indicates the position of the modern SMT. In this case, we define SMT by the depth of obviously enhanced AOM. The vertical extension of AOM zone above the SMT is confirmed directly by the highest methane depletion within the interval 10-30 cmbsf and indirectly - by conservative distribution of $\delta^{13}C$ CH_4 below 30 cmbsf with no signs of AOM-linked isotopic fractionation (Whiticar, 1999). Unfortunately, lack of $\delta^{13}C$ CH_4

data in the subbottom depths < 30 cmbsf caused by insufficient methane concentration, does not allow tracing the expected oxidation shift above 30 cmbsf. At the same time, observed sulfate retaining below the established SMT (values don't decrease below 1.5 mM) indicates no basic conditions for methanogenesis. Elevated sulfate content below the SMT is often caused by natural reoxidation of sulfide under cryptic sulfur cycle operation (Holmkvist et al., 2011; Treude et al., 2014). However, in the studied core, extremely shallow SMT and the uneven boundary between sulfate and methane zone are more likely linked to pore water mixing as result of fresh water fluid flow.

Chloride and pore water mixing

Downcore distribution of biochemically inert pore water chloride is widely used for tracing the variations in pore water salinity indicative of conservative mixing due to fluid migration (Kastner et al., 2008; Pohlman et al, 2008). Chloride concentration in T-04 demonstrates 78% decrease (from 536.36 to 121.87 mM) (Fig. 3). Concave up shape of chloride profile indicates advection-dominated flux with particular subsurface curvature defining the upper limit of a mixing zone at 10 cmbsf (Fig. 3) (Schlüter et al., 2004). Discrimination between the effects of diagenetic reactions and conservative mixing on distribution of the involved pore water solutes are available from the mixing diagram (Pohlman et al., 2008) (Fig 4.). The observed linear correlation between sulfate and chloride reveals physical mixing as a major factor of sulfate depletion. Along with the significant mixing effect, the coinciding excursions of SO_4^{2-} (negative) and Talk (positive) obviously exhibit the effect of AOM. Absence of authigenic carbonates in the sediment core T-04 indicates that odd decrease in pore water Talk at 30 cmbsf is not driven by consumption during CO_2 reduction, instead it probably reflects the dilution through conservative mixing. Thus, chloride distribution indicates upward advection of fresh/brackish water responsible for changing the pore water composition in diagenetic environments.

Considering the basic conditions for fluid transport within the studied sediment section, we cannot ignore the lithological control. The increase of sandy fraction in the lower part of the core indicates the increase in permeability basically required for pore water advection described by Darcy law (Schulz et al., 1994).

Stable isotope composition of methane and its possible sources

The conventional CD diagram based on compilation of $\delta^{13}C$ and δD values can be used for differentiation between the sources of interstitial methane (Whiticar, 1999). In our case, the isotopic signatures in T-04 methane samples are compared with two reference sites (Fig.1, Fig 5). First reference is from methane samples extracted from the ground ice onshore Yamal Peninsula, near Marre Sale (Streletskaya et al., 2018) (Fig. 1a, 5). Second is a marine reference constituted by

methane sampled from gas charged sediment at pingo-like feature site (PLF-2), probably linked to gas hydrate decomposition (Serov et al., 2015).

Isotopic signature of the ground-ice derived methane appears within a transition field of CD diagram apparently indicating coexistence of acetoclastic methanogenesis and CO_2 reduction typical for organic-rich humid landscapes of Arctic tundra (Lofton et al., 2015). In marine conditions, CO_2 reduction becomes the only possible pathway, since as competitive substrate acetate is depleted by SR before entering the zone of methane generation (Whiticar, 1999). Fig. 5 shows that similarly to positive reference values of methane samples from the Marre Sale ground ice, T-04 methane appears within a transitional field with slightly lower values of $\delta^{13}C$ (Fig. 5; black dotted line). Being composed ultimately by the migrated pool, interstitial methane in the target site is likely to involve a remote terrestrial (fresh-water) source partly inheriting its characteristic isotope signatures. In this case, ^{2}H discrimination resulted from a kinetic effect of acetoclastic methanogenesisis, is coupled with utilization of ^{2}H depleted fresh water source for CO_2 reduction pathway. On the contrary, ^{2}H enriched methane from the PLF-2 site, generated exclusively by the CO_2 reduction in typical marine (i.e. sulfate rich) environment shows a corresponding position within CD-plot and provides a negative reference, indicative of different isotopic composition (Fig. 5; blue dotted line) (Whiticar, 1999).

Geochemical data synthesis with implication to the observed fluid migration

Our geochemical analyses indicate presence of dissolved methane flux and fresh/brackish water advection co-occurring within the sediment section. Thus, seismic amplitude blanking anomaly observed on the chirp data is caused by discharge of methane-saturated fresh water fluid. The apparent depth of the seismic amplitude blanking anomaly (> 25 m) indicates a relatively deep location of fluid source connected with the shallow sediment section by sub-vertically developed conduit (Fig 1b).

Possible mechanisms explaining the fluid flow system at T-04 site.

We consider two mechanisms, which may drive the advection-dominated fluid flow system at T-04 site offshore Yamal Peninsula: thawing subsea permafrost and terrestrial ground water discharge.

It has been shown that relict subsea permafrost offshore Yamal Peninsula is an extension of thick organic-rich permafrost complex developed across the western Yamal during ancient sea regressions (Vasiliev et al., 2015; Streletskaya et al., 2018). Therefore, thawing subsea permafrost may drive circulation of methane-charged brackish water initiated by convection between ambient saline water flows and less dense fresh/brackish water from thawing permafrost (salt fingering) (Osterkamp, 2001; Frederick and Buffet, 2015). Shallow drilling into subsea permafrost in the Laptev sea (Buor-Haya bay) (Overduin et al., 2015) showed that excess of dissolved methane released by

thawed permafrost was almost entirely consumed by the AOM immediately above the boundary between unfrozen and frozen sediment sections at the depth of approximately 25 m bellow the seafloor. The insufficient amount of residual methane above the reaction zone was remarkable for dramatic depletion in ^{12}C (Overduin et al., 2015). It is likely that intense advection-dominated methane transport rate significantly overrides the biochemical consumption of dissolved methane in T-04 core. Additionally, the increased buoyancy of methane charged water should stimulate the upward fluid migration driven by density gradient (Park, 1990; Osterkamp, 2001). Similar observations of permafrost-related seabed water discharge are extremely scarce. One of them was detected in the Beaufort Sea, where brackish water discharge has been documented and attributed to seasonal thawing of subsea permafrost; however there was no observations of related methane transport (Dimova et al., 2015).

Alternative mechanism, which may drive the fluid flow at T-04 site, is the subbottom groundwater discharge (SGD). Lateral transportation of methane (as well as other solutes and nutrients) by ground water flows is a well-studied phenomenon (Bugna et al., 1996). Frederick and Buffet (2015) provided a comprehensive numerical model involving SGD related to subsea permafrost at the Beaufort Sea shelf. This model shows that sub-permafrost ground flows can move laterally seaward along the lower permafrost boundary towards its outer edge. There, fresh water flow changes its direction to subvertical providing the quasi-stationary mixing interface significantly further offshore compared to non-permafrost conditions, where the discharge distance is mainly determined by topography-driven hydraulic head (Frederick and Buffet, 2015). In this scenario, continuous permafrost offshore central Yamal Peninsula may reach 45 m isobaths which is significantly more extensive compared to the existing estimate (20 mbsl) (Portnov et al., 2013, Portnov, 2014).

The above scenarios describe two different mechanisms, driving the fluid flow system in the T-04 site offshore Yamal Peninsula. These scenarios are not mutually exclusive, as such, both mechanisms may co-exist, providing complex geochemical signature, which we registered in our sediment samples.

Conclusions

- High resolution seismic amplitude anomaly has been verified by high methane concentration indicating modern shallow fluid flow system offshore Yamal Peninsula.
- Non steady state diagenesis becomes evident from the distribution pattern of reactive compounds suggesting the physical process imposed on local biogeochemical environment. Our data indicate extremely narrow AOM zone with sharp and shallow SMT located at 30 cm subbottom depth with significant temporal variations in methane discharge recorded in pyrite (FeS_2) distribution. Concave up pore water

chloride profile depicts an upward fresh/brakish water advection and the upper limit of subsurface mixing between 5 and 10 cmbsf.

- Terrestrial/fresh water origin of interstitial methane from the sampled location has been revealed by stable isotopic signatures ($\delta^{13}C$ and δD) similar to methane, extracted from ground ice of adjacent onshore setting used as a reference (Marre Sale site). Thus, the apparent explanation for the detected geochemical features of subsurface migration is pore water advection of fresh/brackish water sufficiently enriched in methane.
- We propose two potential mechanisms driving the observed fluid flow: convection of sub-sea permafrost thaw water and sub-permafrost lateral ground water discharge. The latter may indicate the outer limit of continuous permafrost extent offshore central Yamal Peninsula at 45 mbsl isobath.

Research was partly supported by the RFBR grant 16-05-00979 (to P.S., A.K.).

References

Abrams M. A., 2005. Significance of hydrocarbon seepage relative to sub-surface petroleum generation and entrapment. Mar. Petrol. Geol. Bull. 22, 457–478.

Borowski W. S., Paull C. K., Ussler III W., 1996. Marine porewater sulfate profiles indicate in situ methane flux from underlying gas hydrate. Geology, 24, 655-658.

Bourbonniere R. A. and Meyers P. A., 1996. Sedimentary geolipid records of historicalchanges in the watersheds and productivities of Lakes Ontario and Erie. Limnology and Oceanography, 41, 352–359.

Brothers L. L., Hart P. E., and Ruppel C. D., 2012. Minimum distribution of subsea ice-bearing permafrost on the U.S. Beaufort Sea continental shelf, Geophysical Research Letters, 39 (15), L15501, https//doi.org/10.1029/2012GL052222.

Bugna G. C., Chanton J .P., Cable J. E., Burnett W. C., Cable P. H., 1996. The importance of groundwater discharge to the methane budgets of nearshore and continental shelf waters of the northeastern Gulf of Mexico. Geochimica et Cosmochimica Acta, 60, 4735-4746.

Coffin R., Hamdan L., Plummer R., Smith J., Gardner J., Wood W. T., 2008. Analysis of methane and sulfate flux in methane charged sediments from the Mississippi Canyon, Gulf of Mexico. Mar. Petrol. Geol., 25, 977-987.

Coffin R., Smith J., Plummer R., Yoza B., Larsen R., Millholland L., Montgomery M., 2013. Spatial variation in shallow sediment methane sources and cycling on the Alaskan Beaufort Sea Shelf/Slope. Marine and Petroleum Geology, 45, 186-197.

Dimova N., Paytan A., Kessler J. D., Sparrow K., Kodovska F. G.-T., Lecher, A. L., Murray J. and Tulaczyk S. M., 2015. Current Magnitude and Mechanisms of Groundwater Discharge in the Arctic: Case Study from Alaska Environ Sci Technol. Oct 6; 49(20), 12036-43, https//doi.org/ 10.1021/acs.est.5b02215

Frederick J. M. and Buffett B. A., 2015. Effects of submarine groundwater discharge on the present-day extent of relict submarine permafrost and gas hydrate stability on the Beaufort Sea continental shelf, J. Geophys. Res. Earth Surf., 120, 417-432, https//doi.org/10.1002/2014JF003349.

Holmkvist L., Ferdelman T. G. and Jørgensen B. B., 2011. A cryptic sulfur cycle driven by iron in the methane zone of marine sediments (Aarhus Bay, Denmark). Geochim. Cosmochim. Acta 75, 3581–3599.

Iversen N. and Jørgensen B. B., 1985. Anaerobic methane oxidation rates at the sulphate–methane transition in marine sediments from Kattegat and Skagerrak (Denmark). Limnol. Oceanorg. 30, 944–955.

Jørgensen B. B., 2006. Bacteria and marine biogeochemistry, edited by: Shulz, H. D. and Zabel, M., Mar. Geochem., 169–206.

Jørgensen B., Weber A., Zopfi J., 2001. Sulfate reduction and anaerobic methane oxidation in Black Sea sediments. Deep-Sea Research, I 48, 2097-2120

Kastner M., Claypool G. E., Robertson G., 2008. Geochemical constraints on the origin of the pore fluids and gas hydrate distribution at Atwater Valley and Keathley Canyon, Northern Gulf of Mexico. Mar. Petr. Geol., 25, 860–872.

Koch K., Knoblauch C. and Wagner D., 2009. Methanogenic community composition and anaerobic carbon turnover in submarine permafrost sediments of the Siberian Laptev Sea, Environ. Microbiol., 11(3), 657–668, https//doi.org/10.1111/j.1462-2920.2008.01836.x.

Krylov A. A., Ivanov G. I., and Sergeeva E. I., 2005. Recent Sedimentation in the St. Anna Trough (Kara Sea). Oceanology. Vol. 45, No. 1. P. 99-107.

Lapina N. N., 1977. Method for Studying the Matter Composition of the Bottom Sediments (By the Example of the Arctic Ocean) (Nedra, Leningrad, 1977) [in Russian].

Latour, P., Hong, W.-L., Sauer, S., Sen, A., Gilhooly III, W. P., Lepland, A., and Fouskas, F., 2018. Dynamic interactions between iron and sulfur cycles from Arctic methane seeps, Biogeosciences Discuss., https://doi.org/10.5194/bg-2018-223, in review,

Lin Q., Wang J S, Algeo T. J, Sun F., Lin R., 2016. Enhanced framboidal pyrite formation related to anaerobic oxidation of methane in the sulfate-methane transition zone of the northern South China Sea. Marine Geology, 379, 100-108.

Lofton D. D., Whalen S. C. and Hershey A. E., 2015. Polar Biol. 38 (6), 815-827, https//doi.org/10.1007/s00300-014-1641-4.

McGuire A. D., Anderson L. G., Christensen T. R., Dallimore S., Guo L., Hayes D. J., Heimann M., Lorenson T. D., Macdonald R. W. and Roulet N., 2009. Sensitivity of the carbon cycle in the Arctic to climate change. Ecol. Monogr., 79, 523–555, https//doi.org/10.1890/08-2025.1.

Meister P., Liu B., Timothy G., Ferdelman A. Jørgensen B., Khalil A., 2013. Control of sulfate and methane distributions in marine sediments by organic matter reactivity. Geochimica et Cosmochimica Acta, 104, 183–193.

Osterkamp T. E., 2001. Sub-sea permafrost, in Encyclopedia of Ocean Sciences, vol. 5, edited by J. H. Steele, S. A. Thorpe, and K. K. Turekian, 2902–2912, Acad. Press, New York, and London.

Overduin P. P., Liebner, S., Knoblauch C., Günther F., Wetterich S., Schirrmeister L., Hubberten H.-W. and Grigoriev M. N., 2015. Methane oxidation following submarine permafrost

degradation: Measurements from a central Laptev Sea shelf borehole, J. Geophys. Res. Biogeosci., 120, 965–978, https//doi.org/10.1002/2014JG002862.

Park A., 1990. Cellular and oscillatory self-induced methane migration. A. Park, T. Dewers, P. Ortoleva. Earth-Sci. Rev., 29, 249-265.

Peters K. E., Walters C. C., Moldowan J., 2008. The Biomarker Guide. Biomarkers and Isotopes in the Environment and Human History, second ed., vol. 1. Cambridge university press 2004, 471 p.

Pohlman J. W., Ruppel C., Hutchinson, D., Downer R. Z., Coffin R. B., 2008. Assessing sulfate reduction and methane cycling in a high salinity pore water system in the northern Gulf of Mexico. Mar. Petr. Geol, 25, 942–951.

Portnov A., Mienert Ju.,Winsborrow M., Andreassen K.,Vadakkepuliyambatta S., Semenov P., Gataullin V., 2018. Shallow carbon storage in ancient buried thermokarst in the South Kara Sea**.** Sci Rep. 2018 Sep 25; 8 (1):14342. doi: 10.1038/s41598-018-32826-z

Portnov A., Smith A., Mienert Ju., Cherkashov G., Rekant P., Semenov P., Serov P., 2013. Widespread gas release limited by the 20-m isobath at the South Kara Sea Shelf. Gephysical Research letters, 40, 3962-3967.

Portnov A., Mienert Ju., Serov P., 2014. Modeling the evolution of climate sensitive Arctic subsea permafrost in regions of extensive gas expulsion at the West Yamal shelf. J. Geophys. Res. Biogeosci., 119, 2082–2094, https//doi.org/10.1002/2014JG002685.

Rekant P. and Vasiliev A., 2011. Distribution of subsea permafrost at the Kara Sea shelf. Cryosphere of the Earth, XV(4), 69-72.

Rozanov A. G., 2015. Redox System of the Bottom Sediments of the Western Kara Sea. Geochemistry International, 53, 11, 987–1001, https://doi.org/10.1134/ S001670291511004X.

Rukhin L. B., 1961. Fundamentals of Lithology (Gostoptekhizdat, Leningrad, 1961) [in Russian].

Ruppel, C. D., 2011. Methane hydrates and contemporary climate change, Nat. Ed. Knowledge, 3(10), 29 (Available at http://www.nature.com/ scitable/knowledge/library/methane-hydrates-and-contemporary-climate-change-24314790.)

Sassen R., Roberts H. H., Carney R., 2004. Free hydrocarbon gas, gas hydrate, and authigenic minerals in chemosynthetic communities of the northern Gulf of Mexico continental slope: relation to microbial processes. Chem. Geol., 205, 195–217.

Schlüter M., Sauter E. J., Andersen C. E., Dahlgaard H., Dando P. R., 2004. "Spatial distribution and budget for submarine groundwater discharge in Eckernforde Bay (Western Baltic Sea)". Limnology and Oceanography, 49, 157–167.

Schulz H. D., Dahmke A., Schinzel U., Wallmann K. and Zabel M., 1994. Early diagenetic processes, fluxes and reaction rates in sediments of the South Atlantic. Geochimica et Cosmochimica Acta, 58, 2041-2060.

Secrieru, D. and Oaie, G., 2009. The Relation between the Grain Size Composition of the Sediments from the NW Black Sea and their Total Organic Carbon (TOC) Content. Geo-eco-marina, No 15/2009, 5–11. http://doi.org/10.5281/zenodo.57303

Seiter K., Hensen C., Schröter Jü, Zabel M., 2004. Organic carbon content in surface sediments-defining regional provinces. Deep Sea Research Part I: Oceanographic Research Papers, 51(12), 2001-2026, https//doi.org/10.1016/j.dsr.2004.06.014.

Serov P., Portnov A., Mienert, Ju., Semenov, P., Ilatovskaya P., 2015. Methane release from pingo-like features across the South Kara Sea shelf, an area of thawing offshore permafrost. Journal of Geophysical Research - Earth Surface; 120 (8), 1515 – 1529, ISSN 2169-9003s, https//doi.org/ 10.1002/2015JF003467.

Shakhova N., Semiletov I., Salyuk A., Yusupov V., Kosmach D. and Gustafsson Ö., 2010. Extensive Methane Venting to the Atmosphere from Sediments of the East Siberian Arctic Shelf. Science, 327(5970), 1246-1250, https//doi.org/10.1126/science.1182221.

Stein R. and Fahl K., 2004. The Kara Sea: Distribution, Sources, Variability and Burial of Organic Carbon' in the 'Organic Carbon Cycle in the Arctic Ocean,' Ed. By R. Stein and R. W. Macdonald (Springer, Berlin), 237–266.

Streletskaya I. D., Vasiliev A. A., Oblogov G. E., Semenov P. B., Vanshtein B. G., Rivkina E. M., 2018. Methane in ground ice and frozen sediments in the coastal zone and on the shelf of Kara Sea. Led i Sneg. Ice and Snow. 58 (1), 65–77. [In Russian].

Taylor A. E., 1991. Marine transgression, shoreline emergence: Evidence in seabed and terrestrial ground temperatures of changing relative sea levels, Arctic Canada. Journal of Geophysical Research: Solid Earth, 96(B4), 6893-6909, https//doi.org/10.1029/91JB00293.

Treude T., Krause S., Maltby J., Dale A., Coffin R., Hamdan L., 2014. Sulfate reduction and methane oxidation activity below the sulfate-methane transition zone in Alaskan Beaufort Sea continental margin sediments: Implications for deep sulfur cycling. Geochimica et Cosmochimica Acta, 144, 217–237.

Tyson, R.V., 1995. Sedimentary Organic Matter: Organic Facies and Palynofacies; Chapman and Hall, London, 516p.

Vasiliev A. A., Streletskaya I. D., Mel'nikov V. P., Oblogov G. Ye., 2015. Methane in ground ice and frozen Quaternary deposits of Western Yamal. Doklady Akademii Nauk. Proc. of the Academy of Sciences, 465 (5), 604–607 [In Russian].

Vetrov A .A. and Romankevich E. A., 2011. Genesis of Organic Matter in the Kara Sea Bottom Sediments. Oceanology, 51, 4, 649–657.

Whiticar M. J., 1999. Carbon and hydrogen isotope systematics of bacterial formation and oxidation of methane. Chemical Geology, 161 (1), 291-314.

Yamamoto S., Alcauskas J. B., Crozier T. E., 1976. Solubility of methane in distilled water and seawater. J. Chem. Eng. Data, 21, 78–80.

FIGURES CAPTIONS

Fig 1. (a) Location of the offshore sampling station T-04 (this study) and sampling sites at Marre Sale and PLF-2 (Streletskaya et al., 2018; Serov et al., 2015) provided onshore and offshore reference data for comparison of CH_4 stable isotopic compositions; (b) chirp section showing shallow amplitude anomaly in the chirp data; (c) Lithology and grain-size composition of T-04 sediment core.

Fig. 2. Organic matter (OM) of T-04 sediment core (a) TOC (%) downcore distribution; (b) TOC (%) plotted against clay content in the sediments; (c) distribution of n-alkanes (C_{10}-C_{35}) and isoprenoids (phytane and pristane) in hexane extract of the sediment sampled at 5 cmbsf. The ratio indices (CPI, TAR, Pr/Ph) are specified in the black frame.

Table 1. Interstitial hydrocarbon gases (C_1-C_4) in T-04 sediments (molecular composition and stable isotopic composition of methane ($\delta^{13}C$ and δD))

Fig. 3. Gas geochemistry and pore water chemistry in T-04 sediment core. Grey rectangle indicates a zone of anaerobic oxidation of methane (AOM), grey arrow points at sulfate-methane transition (SMT).

Fig. 4. Mixing diagram (after Pohlman et al., 2008), including sulfate and Talk (mM) plotted as functions of chloride distribution (mM). Coinciding negative excursion of sulfate and positive of Talk are outlined by grey ellipse marking AOM against a background of conservative mixing reflected in linear correlation of chloride and sulfate.

Fig. 5. CD diagram of interstitial methane (after Whiticar, 1999), including the data from T-04 core and published data (ground ice from Marre Sale site and PLF-2) for onshore and offshore reference respectively (Streletskaya et al., 2018; Serov et al., 2015). Brown dashed ellipse shows samples with methane of presumably terrestrial (onshore) origin, while blue dashed ellipse shows samples with methane of typical marine (offshore) genesis.

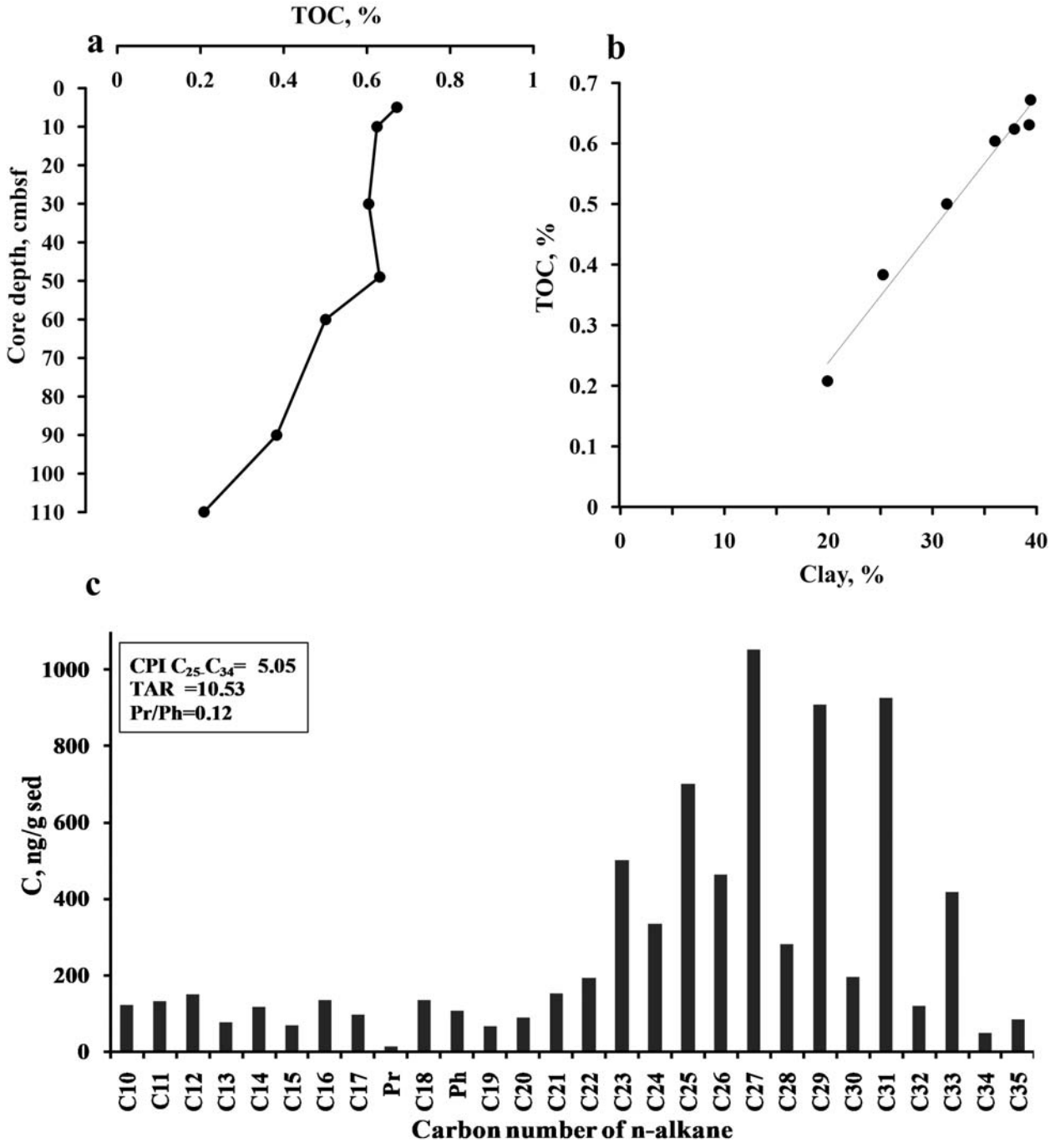
a
TOC, %
0
0.2
0.4
0.6
0.8
1
Core depth, cmbsf
0
10
20
30
40
50
60
70
80
90
100
110
b
TOC, %
0.7
0.6
0.5
0.4
0.3
0.2
0.1
0
0
10
20
30
40
Clay, %
c
CPI C25-C34= 5.05
TAR =10.53
Pr/Ph=0.12
C, ng/g sed
1000
800
600
400
200
0
C10
C11
C12
C13
C14
C15
C16
C17
Pr
C18
Ph
C19
C20
C21
C22
C23
C24
C25
C26
C27
C28
C29
C30
C31
C32
C33
C34
C35
Carbon number of n-alkane

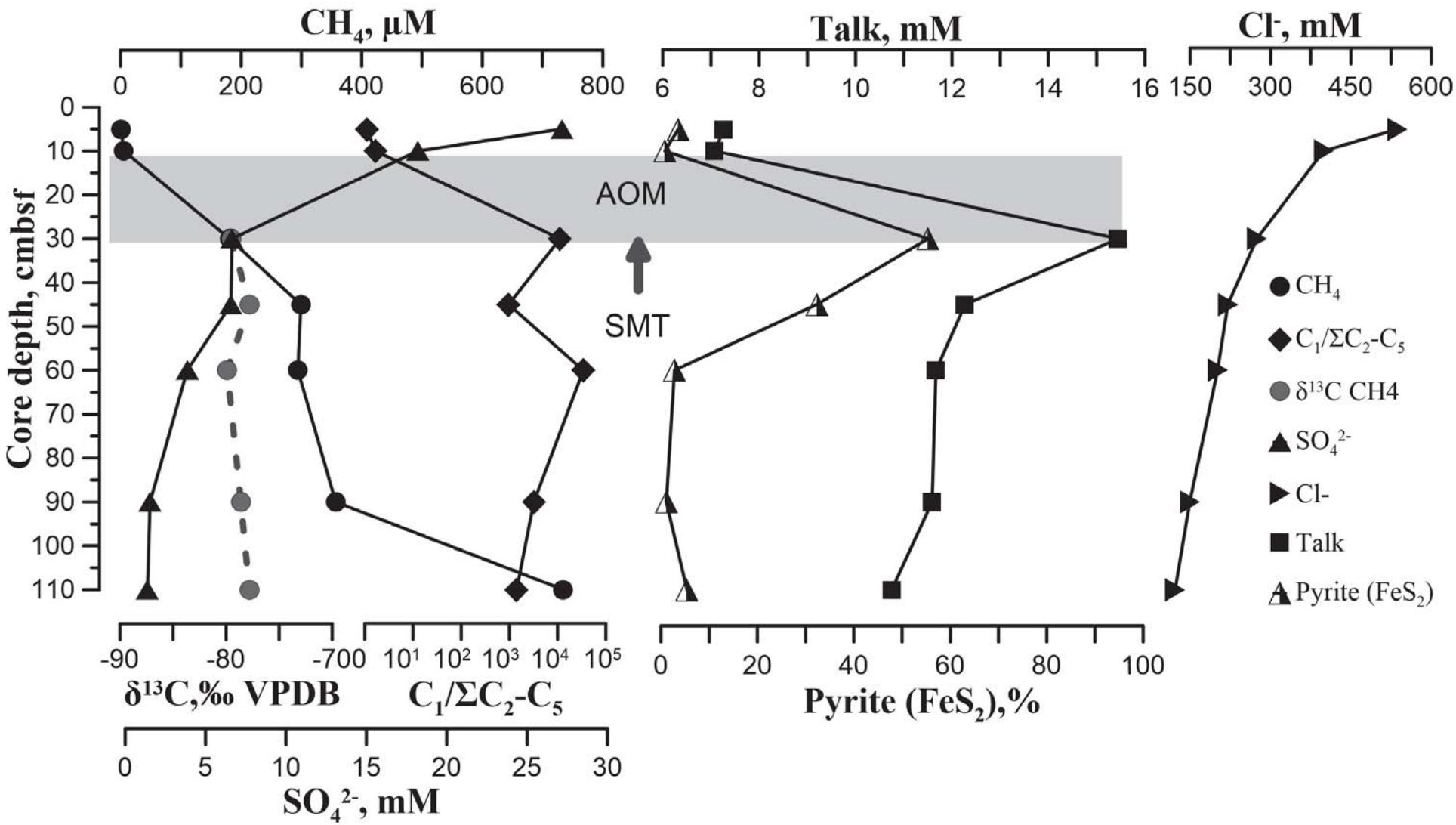
CH4, µM
0
200
400
600
800
Talk, mM
6
8
10
12
14
16
Cl-, mM
150
300
450
600
Core depth, cmbsf
0
10
20
30
40
50
60
70
80
90
100
110
AOM
SMT
CH4
C1/ΣC2-C5
δ13C CH4
SO4 2-
Cl-
Talk
Pyrite (FeS2)
-90
-80
-700
10¹
10²
10³
10⁴
10⁵
δ13C,‰ VPDB
C1/ΣC2-C5
0
5
10
15
20
25
30
SO4 2-, mM
0
20
40
60
80
100
Pyrite (FeS2),%

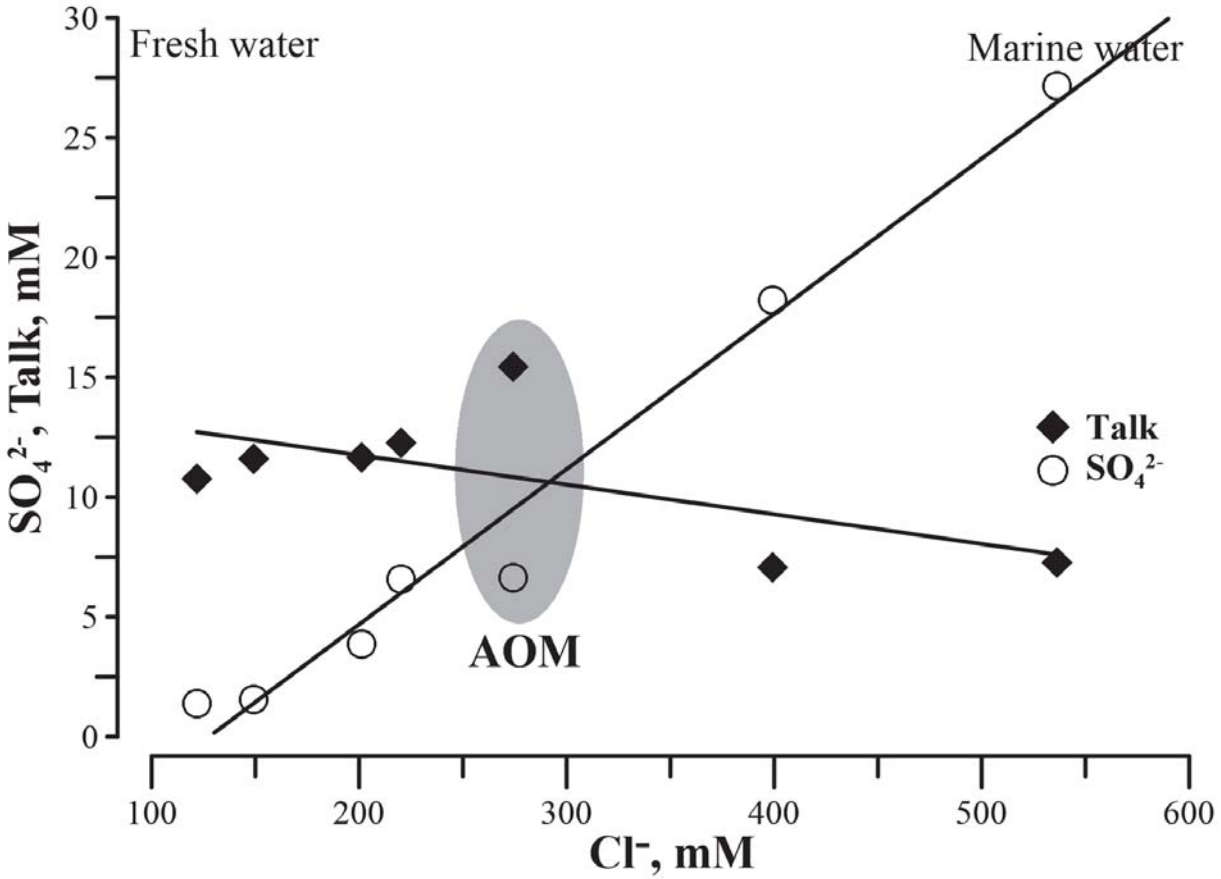
Fresh water
Marine water
AOM
Talk
SO_4^{2-}
SO_4^{2-}, Talk, mM
Cl^-, mM
0
5
10
15
20
25
30
100
200
300
400
500
600

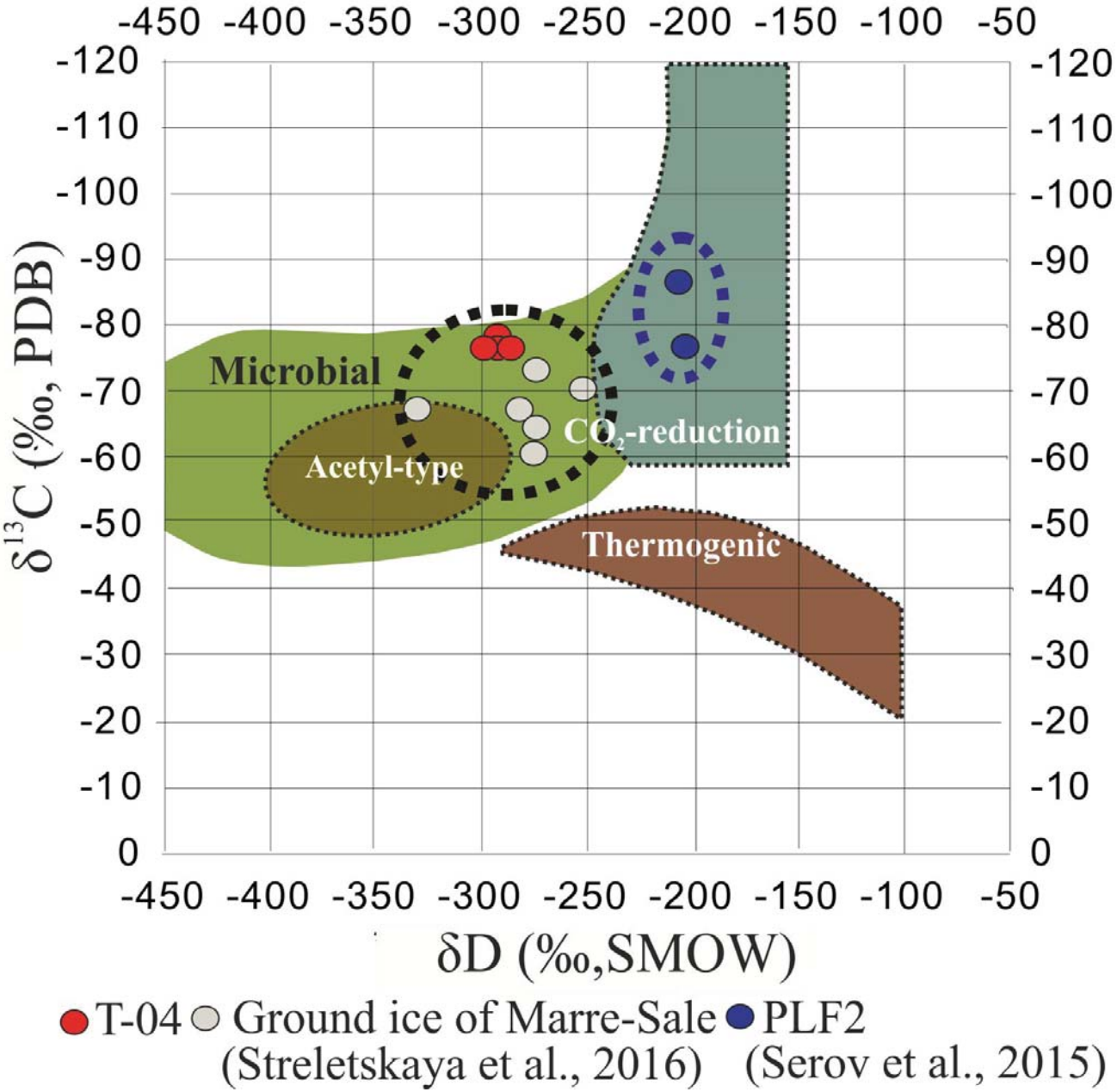
-450 -400 -350 -300 -250 -200 -150 -100 -50
-120 -110 -100 -90 -80 -70 -60 -50 -40 -30 -20 -10 0
δ13C (‰, PDB)
Microbial
CO2-reduction
Acetyl-type
Thermogenic
δD (‰,SMOW)
T-04
Ground ice of Marre-Sale (Streletskaya et al., 2016)
PLF2 (Serov et al., 2015)

Subbottom depth, cm	5	10	30	45	60	90	110
Methane CH_4, µM	0.87	5.42	180.80	168.96	298.26	356.78	734.39
Ethane C_2H_6, nM	6.65	10.99	24.08	37.41	42.81	73.39	107.08
Ethylene C_2H_4, nM	3.87	3.35	4.13	2.69	4.46	6.17	15.79
Propane C_3H_8, nM	4.36	5.59	6.74	10.10	9.23	11.02	55.51
Propylene C_3H_6, nM	0.67	1.40	2.60	1.45	2.47	3.61	3.90
i-Buthane i-C_4H_{10}, nM	1.67	1.22	2.92	1.85	2.65	3.36	23.72
n-Buthane n-C_4H_{10}, nM	1.86	1.66	2.70	1.74	2.76	2.67	24.07
i-Buthylene i-C_4H_8, nM	1.57	1.08	1.47	1.42	1.42	1.60	3.22
$C_1/\Sigma C_2$-C_5	43	215	4051	2983	4534	3505	3149
$\delta^{13}C$, ‰ PDB			-22	-16.4	-12.7	-14.95	-30
δD, ‰ SMOW			-287	-288	-296	-295	-281